SCIENCE ROBOTICS | RESEARCH ARTICLE

SOFT ROBOTS

Crawling, climbing, perching, and flying by FiBa soft robots

Terry Ching[1,2,3]†, Joseph Zhi Wei Lee[1,2], Shane Kyi Hla Win[1], Luke Soe Thura Win[1], Danial Sufiyan[1], Charlotte Pei Xuan Lim[1], Nidhi Nagaraju[1,2], Yi-Chin Toh[4,5], Shaohui Foong[1], Michinao Hashimoto[1,2]*

This paper introduces an approach to fabricating lightweight, untethered soft robots capable of diverse biomimetic locomotion. Untethering soft robotics from electrical or pneumatic power remains one of the prominent challenges within the field. The development of functional untethered soft robotic systems hinges heavily on mitigating their weight; however, the conventional weight of pneumatic network actuators (pneu-nets) in soft robots has hindered untethered operations. To address this challenge, we developed film-balloon (FiBa) modules that drastically reduced the weight of soft actuators. FiBa modules combine transversely curved polymer thin films and three-dimensionally printed pneumatic balloons to achieve varied locomotion modes. These lightweight FiBa modules serve as building blocks to create untethered soft robots mimicking natural movement strategies. These modules substantially reduce overall robot weight, allowing the integration of components such as pumps, valves, batteries, and control boards, thereby enabling untethered operation. FiBa modules integrated with electronic components demonstrated four bioinspired modes of locomotion, including turtle-inspired crawling, inchworm-inspired climbing, bat-inspired perching, and ladybug-inspired flying. Overall, our study offers an alternative tool for designing and customizing lightweight, untethered soft robots with advanced functionalities. The reduction of the weight of soft robots enabled by our approach opens doors to a wide range of applications, including disaster relief, space exploration, remote sensing, and search and rescue operations, where lightweight, untethered soft robotic systems are essential.

INTRODUCTION

Biological systems in nature have evolved to thrive in complex and unstructured environments by relying on soft, elastic, and flexible materials (*1*, *2*). The emerging field of soft robotics aims to bridge the gap between rigid robotic systems and the pliable nature of living organisms, focused on improving the robotic mimicry of organic organisms (*3*). Such organisms include worms, octopuses, geckos, and frogs, each of which uses locomotive strategies tailored to their specific environment (*4*–*7*). The potential for robots with soft bodies is immense: Their flexibility enables them to navigate constricted spaces that are inaccessible to their stiff-bodied counterparts, which may be crucial during disaster relief, space exploration, and other scenarios not suitable for traditional robotic systems (*8*, *9*). Furthermore, the compliant nature of soft robots enables them to work safely alongside humans, minimizing the risk of injury in case of accidental collisions. We characterized soft robots as a whole system using flexible and deformable materials in their construction, such as flexible plastics, elastomers, and other compliant substances (*10*).

Current demonstrations of soft robots rely on external electrical or pneumatic power sources connected through physical tethers (*11*). These physical tethers restrict movement and limit the range of the robots. Untethering soft robotics from electrical or pneumatic power remains one of the prominent challenges within the field (*8*, *12*). There are limited examples of untethered soft robots (*6*, *13*–*18*). Overcoming this challenge to establish functional untethered soft robotic systems hinges on weight reduction of these systems. Some efforts have focused on developing lightweight power components (*19*). Alternatively, the soft actuators themselves, a major contributor to the weight of soft robotic systems, are a target for weight reduction. Pneumatic network actuators (pneu-nets) are one common design of soft actuators (*20*–*25*). Various embodiments of pneu-nets—such as fiber-reinforced (*26*–*31*), multimaterial (*32*–*34*), buckling (*35*, *36*), origami-inspired (*37*–*40*), and fabric/textile (*41*–*43*) soft actuators—are noteworthy in this context. Pneu-nets consist of pneumatically actuating constructs primarily made of silicone rubbers (*20*). Because silicone rubber is a dense material (~1070 kg/m^3), using pneu-nets increases the overall weight of the robot, posing challenges to untethered operations, especially when combined with additional electronic and power components (*11*). A comparison of two representative pneumatically driven, untethered soft robotic systems shows that the weight of the hardware for actuation occupies a substantial percentage (more than 67%) of the weight of the overall robot (table S1) (*15*, *18*). Typically, pneu-net actuators alone can weigh more than 500 g (*6*, *13*–*18*). The increase in the weight of the robotic systems correlates with higher power consumption, thereby limiting the systems' operational capabilities. The weight dilemma is particularly critical for untethered aerial robots, because heavy actuators would render them unviable for mounting on flying machines or constructing entire wings using pneu-nets given the immense power consumption required for maintained flight (*44*).

In this research, we aimed to reduce the weight of soft robots to achieve untethered operation by proposing an alternative design for soft actuators (Movie 1). The redesigned actuators incorporate two critical components: a three-dimensional (3D)–printed pneumatic balloon and a polymer film with transversal curvature, collectively termed FiBa (film-balloon) modules. A transversal curvature locally

---

[1]Pillar of Engineering Product Development, Singapore University of Technology and Design, Singapore, Singapore. [2]Digital Manufacturing and Design Centre, Singapore University of Technology and Design, Singapore, Singapore. [3]Department of Biomedical Engineering, National University of Singapore, Singapore, Singapore. [4]School of Mechanical, Medical and Process Engineering, Queensland University of Technology, Brisbane, Australia. [5]Centre for Biomedical Technologies, Queensland University of Technology, Kelvin Grove, Australia.
*Corresponding author. Email: hashimoto@sutd.edu.sg
†Present address: Department of Biomedical Engineering, Boston University, Boston, MA 02215, USA, and Wyss Institute for Biologically Inspired Engineering, Harvard University, Boston, MA 02115, USA.

Movie 1. Overview of FiBa soft robotic actuators, highlighting their ability to replicate diverse locomotion modes.

imparts anisotropic rigidity to the film without increasing its weight and volume (*45*), which can be displaced by inflating balloons to generate different locomotions in the soft robots. The integration of the films and balloons enabled the creation of both bending actuators and beams with variable stiffness. FiBa modules drastically reduced the overall weight (less than 10 g for each actuating unit), making it possible to add lightweight pneumatic pumps, batteries, and a control board to realize untethered operations. We demonstrated the versatility of FiBa modules through four modes of untethered, biomimetic locomotion: turtle-inspired crawling, inchworm-inspired climbing, bat-inspired perching, and ladybug-inspired flying. Crucially, the demonstration of flying machines was ensured only with the reduced weight of the actuator enabled by FiBa modules. Overall, this work designed a method of fabricating lightweight, untethered soft robots capable of (but not limited to) mimicking four basic modes of locomotion: crawling, climbing, perching, and flying. Crucially, biomimetic structures and locomotion can be rapidly prototyped by redesigning the films and repositioning the FiBa modules, offering limitless customizability to mimic the complex locomotion of living organisms.

RESULTS

Experimental design

Existing pneu-nets made entirely of silicone exhibit a notable weightiness, making it challenging to incorporate additional power and control components to achieve untethered operation (*8*, *11*, *12*). Successful development of untethered soft robots requires further innovations in lightweight materials and actuator design. Here, we designed lightweight components to create actuators that we termed FiBa modules. We investigated two strategies to reduce the overall weight of the actuators. The first strategy involved using thin films as lightweight structural components, and the second strategy focused on using stiff silicone to decrease the weight of the pneu-nets. Simple modifications of thin-film polymer sheets via origami and kirigami approaches (for example, cutting, folding, and rolling) enable us to shape the films into desired configurations, facilitating the mimicry of natural locomotions.

To enhance the effectiveness of thin-film polymer sheets as structural components, we introduced transversal curvature to increase the stiffness of thin-film polymer sheets (*45*, *46*). A single flat sheet of material is prone to twisting and bending. For example, a sheet suspended as a cantilever drastically deflects downward when a force is applied to the end of the cantilever (Fig. 1Ai). However, by incorporating transversal curvature similar to that found in a spring-return tape measure or party blow horn, the film achieved increased bending resistance. When a force was applied to the end of a cantilever with a transversal curvature, the resulting film bending deflection was notably diminished (Fig. 1Aii). When the concave surface of the curvature was oriented upward, the bending deflection was reduced further, highlighting the anisotropic rigidity of curved films (Fig. 1Aiii). Using transversal curvatures, we selectively added stiffness into the films to serve as either structural components or actuators.

In addition to the use of transversal curvatures, we fabricated the pneu-nets using silicone with a high modulus of elasticity to reduce the weight of the robot. For instance, pneu-nets–based soft robots in reported studies use Ecoflex with a maximum modulus (at 100% elongation) of ~82.7 kPa (*6*, *22*, *25*). Instead, this work used Dragon Skin 30, a silicone rubber from Smooth-On, which exhibits a modulus of ~593 kPa. The use of the stiffer material allowed for reduction of the mass of materials required to achieve the same strength.

By integrating curved thin films with 3D-printed silicone balloons made from Dragon Skin 30 (Fig. 1B), we demonstrated two primary building blocks for soft robots: the FiBa bending module and the FiBa variable stiffness beam module. These FiBa actuators served as the basic building block for the soft robots demonstrated in this study. To create a FiBa bending module, we sandwiched a modular balloon between two polymer films in a curved configuration. We reproducibly demonstrated bending motion when the balloon was pneumatically inflated (Fig. 1C). The modular balloons were pneumatically coupled together using polytetrafluoroethylene tubing and silicone tubing of various sizes (fig. S1). Similarly, FiBa variable stiffness beam modules were created when combining two polymer sheets with a modular balloon (Fig. 1D). When deflated, the beam was foldable and rollable. However, when the balloon was inflated, the beam gained structural stiffness as the balloon exerted radial pressure on the inner surface of the polymer thin film, inducing a curvature that induced increased structural integrity to the beam.

By using the FiBa modules as building blocks, we drastically reduced the weight of the soft robots, allowing for the addition of additional payload for untethered operations. The untethered operation of pneumatic-powered soft robots requires the addition of electronic components such as a small pneumatic pump (~6 g), micro pneumatic valves (~5 g each), a battery (~9 g), and a microcontroller (~3 g). We demonstrated fully untethered operations such as crawling, climbing, perching, and flying. Although this work focused on demonstrating four specific modes, the versatility of these FiBa actuators allows for adaptation to mimic a wide range of other locomotion modes.

Rigidity by curvature

The curvature of the thin film resulted in bending anisotropy. The anisotropic rigidity of transversally curved thin film has been studied in existing literature (*45*, *47*–*49*), and our simulation results validated these findings (fig. S2). The transversely curved surface (Fig. 1A, ii and iii) exhibited greater resistance to bending compared with a film without transversal curvature (Fig. 1Ai). The transversely curved surface resisted bending more effectively when force was applied normally to the concave side (Fig. 1Aii) than when applied

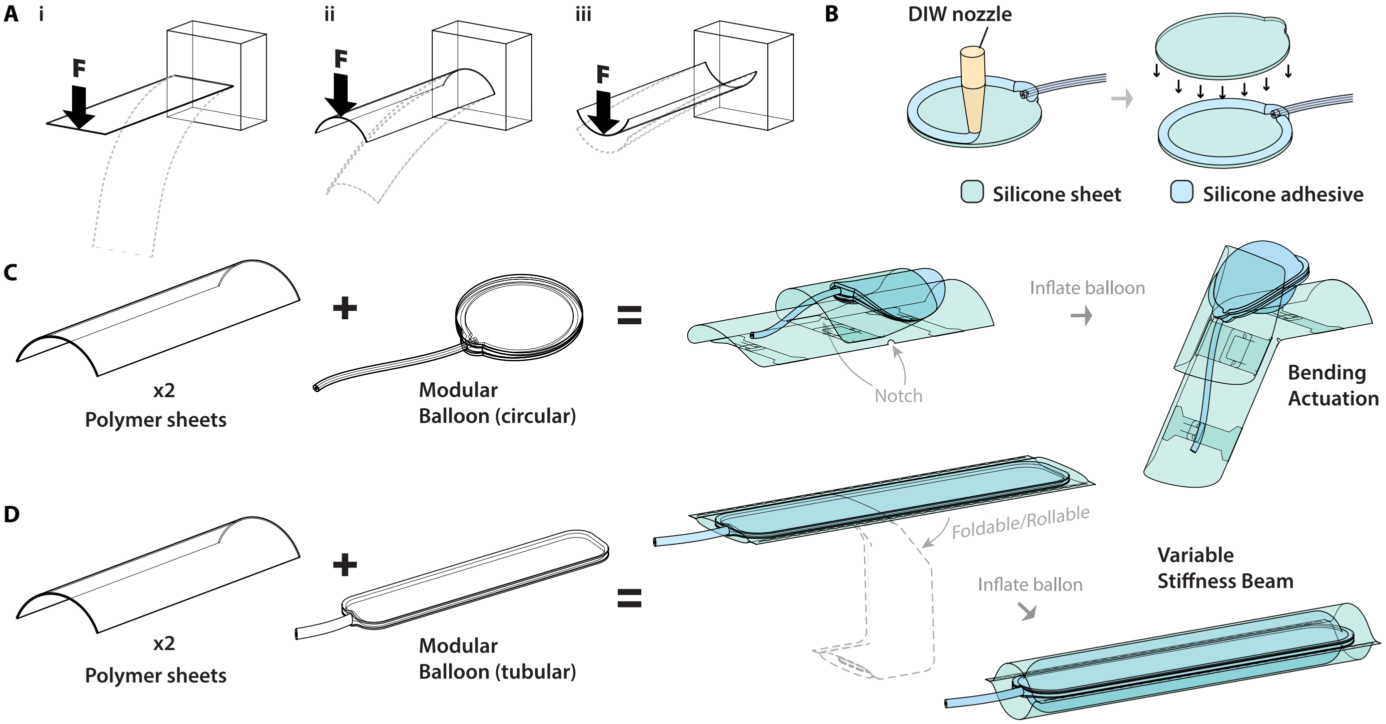

Fig. 1. Illustration of FiBa modules. (**A**) Illustrations depicting the anisotropic bending characteristics under force application: (i) a flat surface with no transversal curve, (ii) a transversally curved surface with force applied to the concave side, and (iii) a transversally curved surface with force applied to the convex side. (**B**) Schematic illustration of the method to fabricate the modular balloon. DIW, direct ink writing. (**C**) Illustration of combining polymer sheets and modular balloons to form the FiBa bending actuator. (**D**) Illustration of combining polymer sheets to form the FiBa variable stiffness beam.

to the convex side (Fig. 1Aii). This crucial feature enables the working of the FiBa bending module. When the balloon between the two curved surfaces was inflated, the bending anisotropy resulted in bending only in one direction. To limit the bending to a predetermined region on the polymer sheet, two small notches were incorporated on either side (Fig. 1C). The notches functioned as localized compliant hinges. Hence, the bend always occurred along the notch-induced weakness when the balloon was inflated (*50*). The structure was required to revert to its original state when the balloon was deflated for repeated actuation cycles. As the structure was bent, it stored up elastic potential energy, allowing it to spring back to its original state when the balloon was deflated.

To understand the behavior of the structure with varying degrees of curvature, we investigated the effect of curvature on the spring force. This refers to the elastic potential energy of the structure that assists in returning it to its original shape when the applied bending force is removed. Our study focused on how different curvatures influenced this restorative spring force when the structure was bent. All five sets of specimens have the same arc length (S = 32 mm) (Fig. 2A). However, the five sets have different chord lengths (C = 22, 24, 26, 28, and 30 mm) (Fig. 2A). A shorter chord length is indicative of a greater degree of curvature. A self-locking mechanism was incorporated into the polymer thin film (fig. S3). Before the bending test, we prestressed the structure by repeatedly bending it from 0° to 90° 10 times. Prestressing the structure ensured that the measured values represent a bending actuator subjected to multiple loading conditions after repeated usage. Our measurement suggested that, although the fatigue weakening after the initial bending was apparent, there was no observable weakening effect after many cycles of bending (n = 100, 200, and 300) (fig. S4 and Supplementary Methods). We therefore used the prestressed sample (n = 10) as the specimens for all subsequent measurements.

The bending test results of the specimens are summarized (Fig. 2, B and C). We observed the following trend for all of the specimens when the test was performed on the concave side: The measured load peaked at ~5-mm extension and dropped gradually until ~10-mm extension before gently increasing after ~10-mm extension. Generally, we found that a higher curvature resulted in a higher measured load. However, that trend only applied when the chord length was reduced from C = 30 to 26 mm. When the chord length was reduced further, the maximum load at ~5-mm extension was lower than the specimen, C = 26 mm (see Fig. 2B; C = 24 and 22 mm). We found that when C was less than 24 mm, permanent plastic deformation was observed (a permanent crease was formed) after prestressing the sample 10 times (fig. S5). We hypothesize that highly localized plastic deformation occurs readily with lower chord lengths, which weakens the flexural strength of the structure, thus recording lower peak loads than specimen C = 26 mm. As such, C = 24 mm and C = 22 mm were not the preferred choices of curvature in the following demonstration. We required our structures to be able to spring back (sufficient torque, τ) to their original configuration (θ = 0°) for the entire range of the bent angle θ (Fig. 2C). Figure 2C shows that all of the specimens have a torsional spring force of more than 6 N·mm throughout the full range of θ. In other words, throughout the range of θ, it has stored torsional potential energy to spring the structure back to its original position. Empirically, we

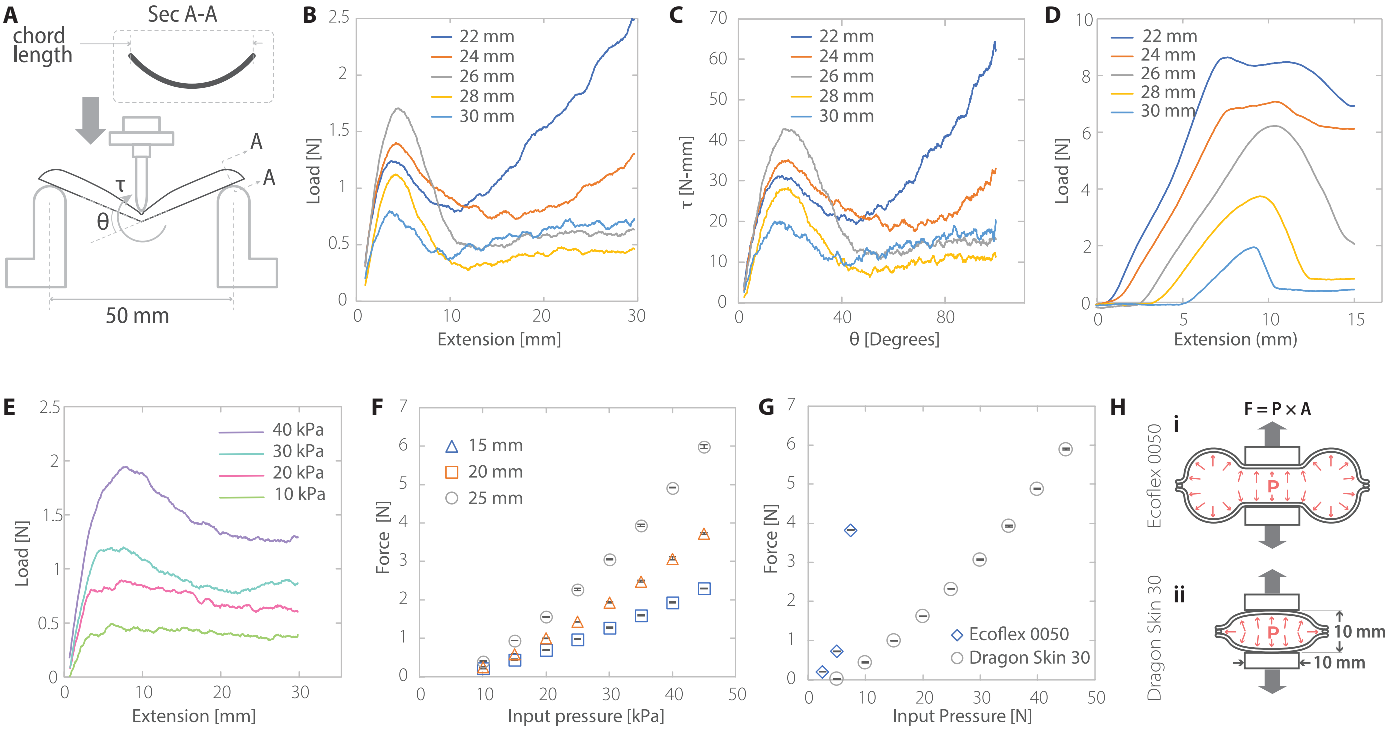

Fig. 2. Characterization of curved structures and modular balloons. (**A**) Schematic illustration of the three-point bending test performed on the curved structures. (**B**) Graph summarizing the flexural strength of the curved structures when the test was performed on the concave side with relation to extension. (**C**) Graph summarizing resultant structural torsional force τ_s relative to a given angle θ. (**D**) Graph summarizing the flexural strength of the curved structures when the test was performed on the convex side. (**E**) Graph summarizing the flexural strength of the FiBa variable stiffness beam with different pressure. (**F**) Mean force (± SEM) of balloons of varying sizes in response to the input pressure ($n = 3$). (**G**) Mean force (± SEM) of balloons made from materials of different stiffness in response to input pressure ($n = 3$). (**H**) Illustration of the expansion characteristics of balloons made from (i) Ecoflex and (ii) Dragon Skin 30. (B to E) $n = 3$ for each line.

found that all the specimens with chord lengths between 22 and 30 mm had sufficient bending stiffness, and they returned back to their original configuration.

To find the suitable degree of curvature for our robots, it is also essential to investigate the maximal bending load that the structure could withstand when the force was applied from the convex side. Sufficient bending stiffness from the convex side is required to prevent undesired structural failure; this is especially important because the curved surfaces have a secondary load-bearing function. The five sets of specimens with varying degrees of curvature were subjected to a three-point bending test from the convex side. We found that a higher degree of curvature resulted in a higher flexural strength (Fig. 2D). A linear increase in load was observed until the structure buckled and failed at an extension of 7 to 10 mm.

Last, we also investigated the bending strength of the variable stiffness beam. The stiffness of the beam was varied by changing the pressure in the tubular balloon (Fig. 2E). We varied the pressure from 10 to 40 kPa while subjecting the beam to the three-point bending test. We observed that a higher pressure resulted in higher flexural strength. For example, when inflated with 10 kPa of pressure, the beam could withstand ~0.5 N before buckling. However, when inflated with 40 kPa of pressure, the beam could withstand up to ~2 N before buckling. Crucially, when no pressure was applied, the variable stiffness beam could be folded and rolled into a compact form factor. When the balloon was inflated by increasing the pressure, the structural rigidity increased. Our robots can adopt this capability to allow them to be folded for storage or transportation and subsequently inflated at the destination for operation.

Force by pneumatics

One of the main advantages of using a pneumatically powered actuator was the ability to generate a relatively large force with a small pressure above atmospheric pressure. The force generated, F, is a function of the applied pressure, P, multiplied by the surface area, A

$$F = P \times A \tag{1}$$

In our setup, the force was translated using a pneumatically inflated balloon. When the balloon was pressurized, it inflated and transmitted force (F) onto the surface it contacts (A). The magnitude of the transmitted force could be varied by changing the P or A. Increasing A would require increasing the size of the entire robot; therefore, it was preferable to increase P instead. It was imperative to select a suitable silicone variant that allowed effective increase of the applied pressure. The maximum permitted pressure of a spherical balloon, $P_{\max}$, is directly proportional to the modulus of elasticity, E, multiplied by the initial thickness of the balloon, t_0, divided by the initial diameter of the balloon, d_0 (*51*–*53*) (Supplementary Methods)

$$P_{\max} \propto \frac{Et_0}{d_0} \tag{2}$$

In other words, three variables could be adjusted to increase the $P_{\max}$: increasing E, the modulus of elasticity of the balloon; increasing t_0, the thickness of the balloon wall; and reducing d_0, the initial diameter of the balloon. Changing the thickness of the balloon wall was not favorable because increasing the thickness would inevitably increase the weight of the system. Similarly, reducing the initial diameter of the balloon was also excluded because it decreased the surface area, thereby lowering the force generated by inflation (Eq. 1). Figure 2F suggests that a balloon with a smaller diameter (15 mm) resulted in a lower transmitted force than a balloon with a bigger diameter (25 mm) when the same internal pressure, P, was applied. Therefore, the preferred method of increasing $P_{\max}$ was to increase the modulus of elasticity of the balloon. To this end, we used Dragon Skin 30 because it has a higher modulus of elasticity (~592.9 kPa) than Ecoflex 00-50 (~82.7 kPa), approximately sevenfold.

Experimentally, we fabricated a balloon (diameter = 25 mm) with Ecoflex 00-50 sheets (thickness = 0.77 mm). We found that the $P_{\max}$ of the Ecoflex 00-50 balloons was ~10 kPa (Fig. 2G). When additional air was pumped into the balloon, it continued to expand without increasing the internal pressure (Fig. 2Hi). As a result, the maximum force that the Ecoflex balloon could translate to the top and bottom surfaces ($10\ \text{mm}^2$ by $10\ \text{mm}^2$) was ~3.9 N. However, when a silicone with a higher modulus of elasticity was used (Dragon Skin 30), we were able to increase the internal pressure steadily up to the upper limit of our micropump (45 kPa) (Fig. 2, G and Hii). Under this condition (internal pressure of 45 kPa), the force translated to the top and bottom surfaces reached ~5.9 N.

We assembled the transversally curved thin film with the Dragon Skin 30 balloons to create a FiBa bending actuator. The bending angle primarily depended on two factors: the applied pressure to the balloon and the number of balloons at the joint. Our initial experiment suggested that the maximum bending angle was less than 60° when only one balloon was used. To allow an increased range of bending, we used two balloons at each joint of the bending actuator for all subsequent works discussed in this paper. The range of the motion of this bending actuator was characterized (figs. S6 and S8B). This actuator was able to achieve the motion between 0° (straight) and 90° (perpendicular) below 30 kPa. This range of input pressure was adequate for the actual operation because the maximum pressure that the miniaturized pump can generate was 45 kPa in our experiment. During the inflation and deflation of the balloons, hysteresis was observed in the actuators, notably for the bending angle of 10° to 50° (with the input pressure of 5 to 10 kPa correspondingly). However, the hysteresis was not apparent for the bending angle greater than 50° (fig. S6).

We compared the performance of our FiBa actuator with that of the pneu-net actuator available in Soft Robotics Tool Kit (*54*). The pneu-net actuator required higher pressure to start bending than the FiBa actuator; this difference could be attributed to the ease of deformation of the FiBa actuator consisting of thin films. At high input pressure (50 kPa), the magnitude of the forces generated by the FiBa actuator and was comparable to that of the pneu-net actuator (fig. S7A). However, the normalization of the attained force by the body mass of the actuator suggested that the FiBa actuator could generate substantially higher forces (by nine times) per mass of the actuating module (fig. S7B). Overall, this experiment highlighted the advantage of the FiBa actuator for performance comparable to those of existing actuators yet with substantially reduced mass of the actuator.

It is crucial to highlight that the micropump 1 in use (fig. S8A) exhibited a comparatively low flow rate, leading to sluggish actuation speed (fig. S8, B and C). This particular micropump was selected because of its low weight (~6 g). Opting for micropumps with higher flow rates would inevitably result in an augmented system weight. This weight increase can be attributed to the necessity for a larger motor, demanding higher power and, consequently, bulkier and heavier battery (fig. S8A). Although a faster actuation response could be achieved using a pump with additional weight (fig. S8C), trade-offs among speed, weight, and power consumption were inevitable.

Turtle-inspired crawling robot

To demonstrate the versatility of our FiBa actuators, we first fabricated an untethered robot that could move on land (movie S1). We took inspiration from the locomotion of a turtle. On land, a turtle uses its front limbs (front flippers) to propel itself forward (Fig. 3A). To mimic the locomotion of a turtle, we used four FiBa bending modules (two balloons in each actuator) and two lifting actuator modules (Fig. 3B). The entire robot was built using kirigami and origami of thin-film polyvinyl chloride (PVC) sheets (thickness = 0.18 mm) and a network of modular balloons pneumatically coupled to pumps and valves. The detailed assembly of the robot (figs. S9 and S10) and the schematic of the fluidic connection (fig. S11) are illustrated in the Supplementary Materials. The four bending FiBa modules served as flippers, acting as the four points of contact with the ground (Fig. 3Ci). The bending motion propelled the robot forward when the balloon was inflated to operate the actuators (Fig. 3Cii). After that, the flippers were returned to their original position. We designed a simple lifting actuator (Fig. 3B) that momentarily lifts the robot off the ground (Fig. 3Ciii). When the balloons in the flippers were deflated, the flippers returned to their original positions. Last, a second pump was used to apply negative pressure to the balloons inside the lifting actuator, allowing the four flippers to contact the ground.

To achieve untethered operation, we used two electric-powered pneumatic pumps (one positive pressure pump and one negative pressure pump, ~6 g each), two valves (~5 g each), a microcontroller (~3 g), and a single-cell lithium-polymer (LiPo) battery (260 mAh, ~9 g) (fig. S12). An infrared (IR) receiver was also incorporated to control the robot remotely. The combined weight of the power and control components was 40 g. The weight of the entire robot was 70 g.

Inchworm-inspired climbing robot

To demonstrate the ability to fabricate an untethered climbing robot, we took inspiration from the locomotion of an inchworm (Fig. 4A). The makeup of the climbing robot consisted of two grasping modules and two bending FiBa modules (two balloons were used in each actuator) (Fig. 4B). The detailed assembly of the robot (figs. S13 and S14) and the fluidic connection (fig. S15) are illustrated in the Supplementary Materials. The grasping module consisted of three modular balloons encased in a circular loop made of PVC thin film (Fig. 4C). When the silicone balloons were inflated, they formed conformal contact with the pole, providing a firm grasping force sufficient to support the weight of the entire robot (68 g). The combined weight of the grasping module and FiBa bending module totaled 14 g; the power and control components totaled 54 g. Our experiments demonstrated the capacity of the robot to climb the pole vertically with the power and control components placed

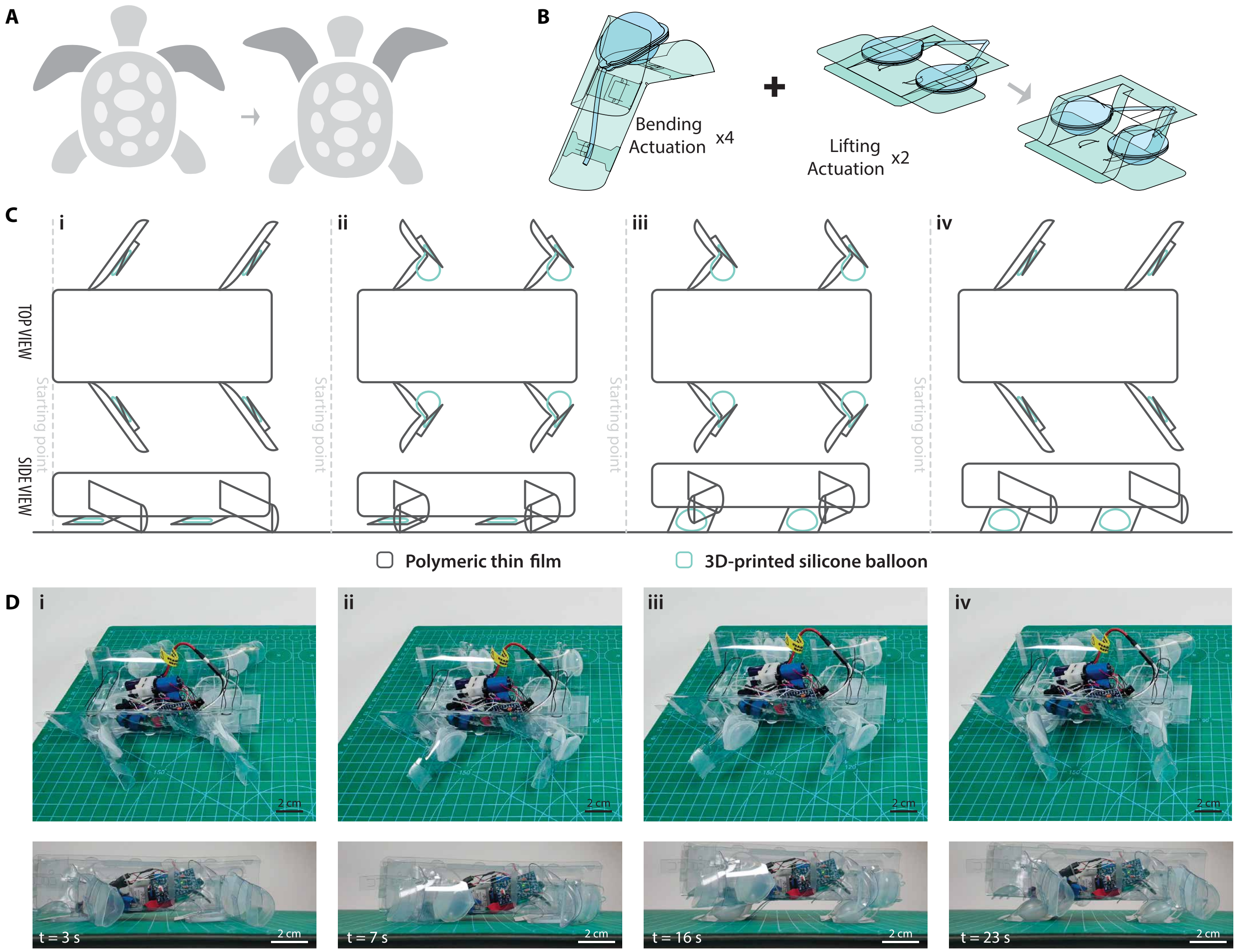

Fig. 3. Turtle-inspired crawling robot. (**A**) Illustration of the locomotion of a turtle. (**B**) Illustration of the actuation modules used in the crawling robots. (**C**) Step-by-step illustration of the locomotion of the crawling robot in one cycle. (**D**) Step-by-step photographs of the locomotion of the crawling robot in one cycle. Scale bar, 2 cm.

underneath for untethered operation (Fig. 4D). Mounting the power and control components directly onto the moving elements (grasping modules or FiBa modules) altered its center of mass, and the overall stability of the climbing robot was compromised. To ensure uninterrupted climbing, we iteratively designed the climbing robot so that the power and control components were positioned to hang underneath the FiBa actuator that performs grasping.

The climbing robot climbs using a six-step process (Fig. 4E, movie S2, and fig. S15). In the first step, the top grasping module was activated by inflating the balloons and providing a firm grip on the pole (Fig. 4Ei). In the second step, the two bending FiBa modules were activated to lift the bottom grasping module and the payload consisting of the power and control components (Fig. 4Eii). In the third step, the bottom grasping module was activated (Fig. 4Eiii). In the fourth step, the top grasping module was deactivated to release the grip on the pole (Fig. 4Eiv). In the fifth step, the bending FiBa module was deactivated, allowing the top grasping module to be raised (Fig. 4Ev). Negative pressure was supplied to the bending actuators in this step to ensure that the balloons were fully deflated. The top grasping module was activated in the sixth step, and the bottom grasping module was deactivated before the cycle was repeated (Fig. 4Evi).

To achieve untethered operation, we used two electrical-powered pneumatic pumps (one positive pressure pump and one negative pressure pump, ~6 g each), four valves (~5 g each), a microcontroller (3 g), and a single-cell LiPo battery (260 mAh, ~9 g) (fig. S12). An IR receiver was also incorporated to control the robot remotely.

Bat-inspired perching robot

Power-to-weight (or thrust-to-weight) ratio is a paramount consideration for aerial robots. Conventional methods of fabricating pneu-net soft robotics grippers by casting usually consist of heavy silicone slabs unsuited for untethered flight (*11*, *15*, *23*, *55*). As a quick comparison, the mGrip (Soft Robotics Inc., Bedford, MA, USA) four-finger gripper weighs more than 270 g. The mGrip grippers were designed primarily for the food processing industry and not for untethered

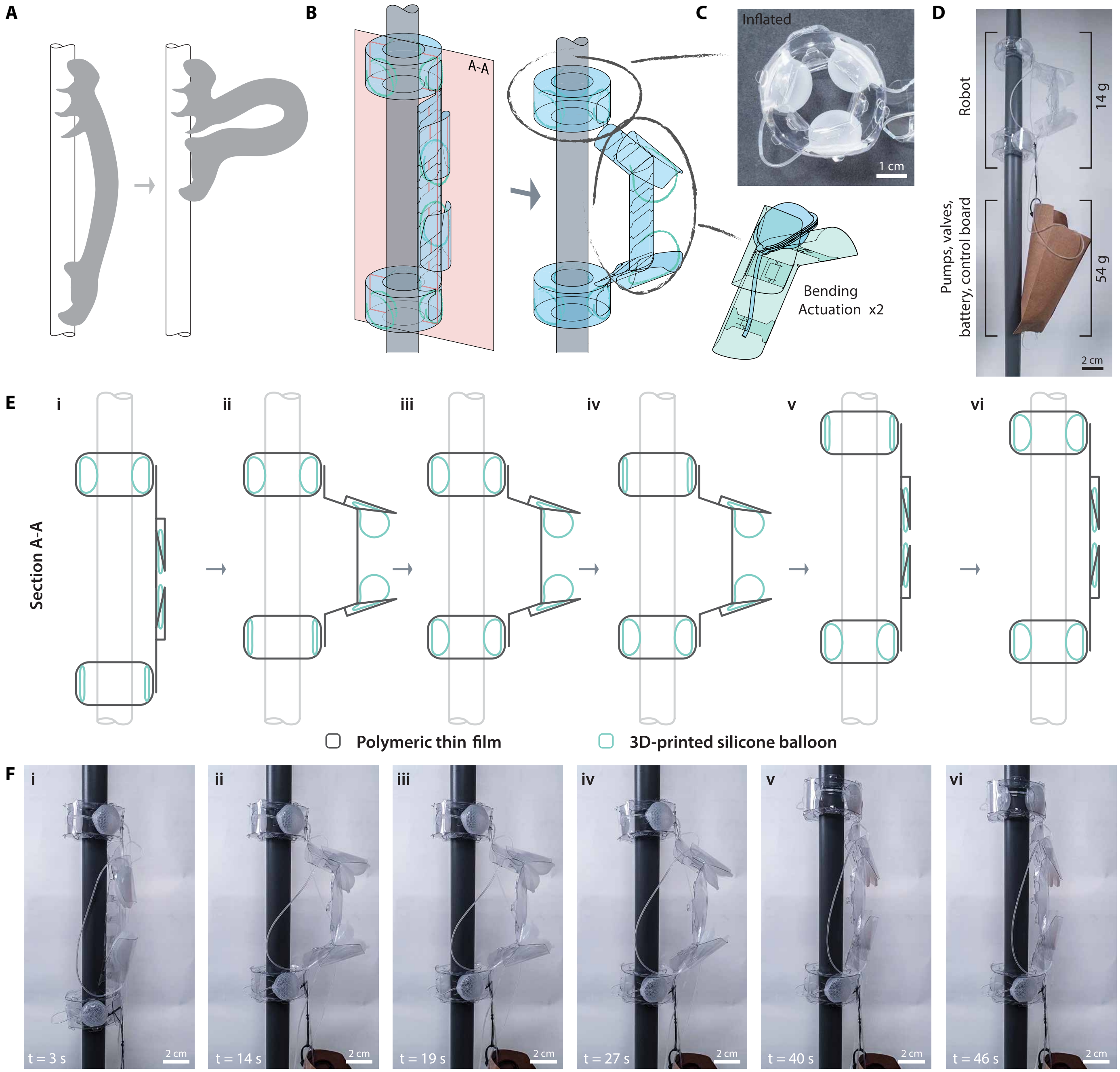

Fig. 4. Inchworm-inspired climbing robot. (**A**) Illustration of the locomotion inchworm. (**B** and **C**) Illustration of the actuation modules used for the climbing robots. (**D**) Photograph of the climbing robot carrying the power and control components to highlight their respective weight. (**E**) Step-by-step illustration of the locomotion of the climbing robot in one cycle. (**F**) Step-by-step photographs of the locomotion of the climbing robot in one cycle. Scale bar, 1 cm (C); 2 cm (D to F).

operations; hence, weight consideration was not a priority. Here, we explored mounting a four-finger gripper on a quadcopter to achieve perching capabilities. We took inspiration from how a bat rests by perching on branches upside down (Fig. 5A). Although aerial robots have proven helpful for remote sensing, inspection, and search and rescue applications (*56*), the limited flight time of most aerial robots (typically less than 1 hour) hinders the practical applications of remote sensing, inspection, and search and rescue. It will thus be beneficial for aerial robots, such as quadcopters, to have the ability to perch and save energy (*56*, *57*).

Using our FiBa modules, we achieved a lightweight gripper. We constructed a four-finger gripper using eight bending FiBa modules (two balloons were used in each actuator) (Fig. 5B). The detailed assembly of the robot (fig. S16) and the fluidic connection (fig. S17) are illustrated in the Supplementary Materials. Each finger consists of two bending actuator modules (Fig. 5C). The combination of the polymer thin film and the modular balloons weighs only 30 g. Including the power and control components, the entire gripper weighs 55 g; this is less than the payload that a commercially available quadcopter can easily carry.

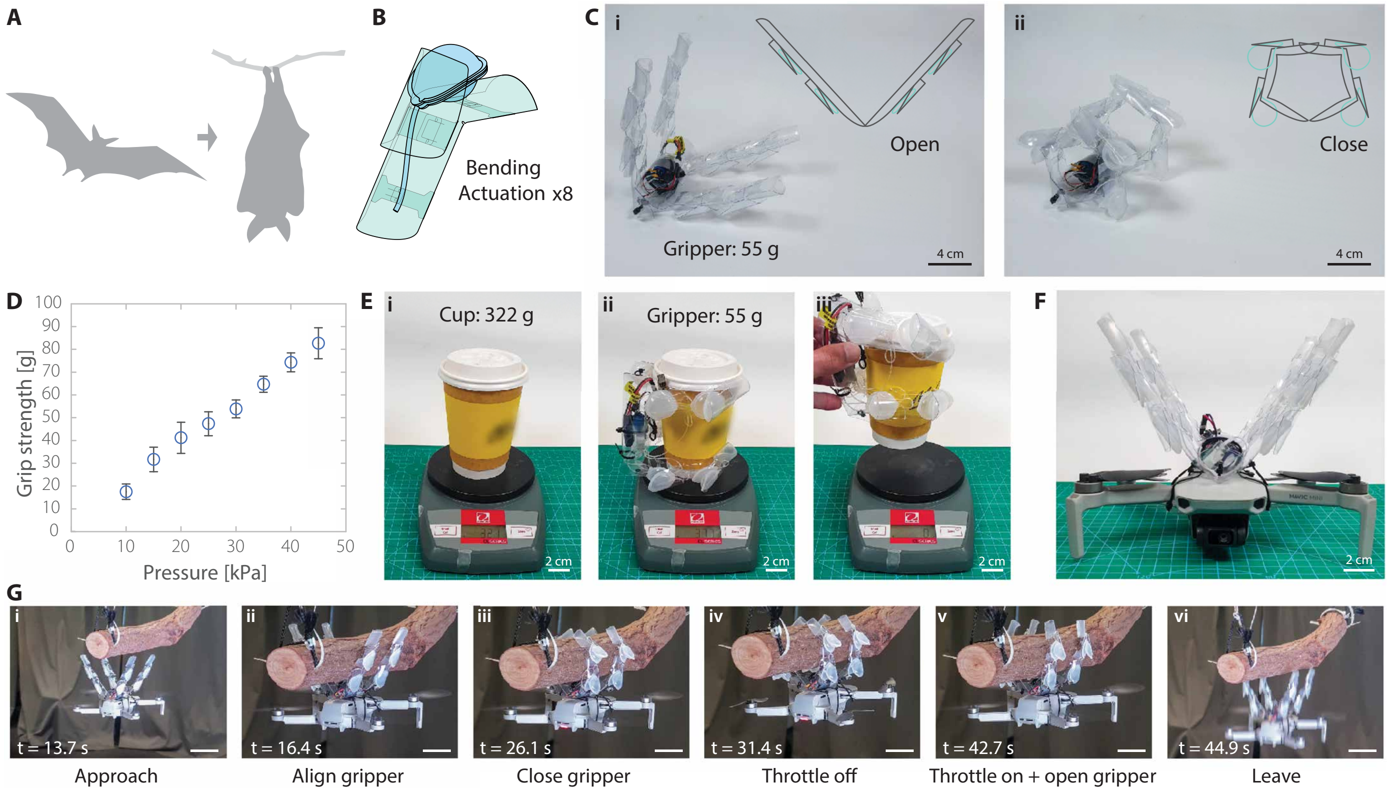

Fig. 5. Bat-inspired perching robot. (**A**) Illustration of the perching motion of a bat. (**B**) Illustration of the actuation modules used for the perching gripper. (**C**) Photograph of the perching gripper in the (i) open and (ii) closed state. (**D**) Mean grip strength (± SEM) of the gripper in response to varying input pressures applied to the modular balloons (*n* = 3). (**E**) Time-lapse photographs demonstrating the ability to grasp a filled cup of coffee. (**F**) Photograph of the perching gripper mounted on a DJI Mavic mini quadcopter. (**G**) Time-lapse photographs of the gripper undergoing perching on a branch. Scale bar, 4 cm (C); 2 cm (E and F); 5 cm (G).

Using a modified weighing scale (fig. S18), we measured the grip force of the gripper with respect to the internal pneumatic pressure. A gripping force of 82.7 g (~0.81 N) was achieved when 45 kPa of pneumatic pressure was applied (the maximum attainable pressure of the pump is 45 kPa). Coupled with silicone sleeves to increase the friction between the gripper and the gripped object, we showed that the gripper could comfortably grip and lift a filled coffee cup weighing 322 g. This demonstration highlighted an untethered gripper capable of carrying five times its weight (movie S3).

Next, we mounted the gripper on a quadcopter. We used a DJI Mavic Mini quadcopter weighting 249 g. The gripper was positioned on the top of the quadcopter to avoid interfering with the flight sensors (for example, obstacle avoidance sensors, ultrasonic sensors, and IR sensors), typically located beneath the quadcopter. The modified DJI Mavic Mini has an additional perching capability to save energy (Fig. 5G and movie S4). The quadcopter was remotely controlled to align the gripper on a tree branch (Fig. 5G, i and ii). Next, the gripper was activated to close its jaws (Fig. 5Giii). After successfully closing the jaws, the quadcopter could throttle off to save energy (Fig. 5Giv). To unperch the quadcopter, the user first turned the throttle on before opening the jaws of the gripper (Fig. 5Gv). After opening the gripper, the user could control the quadcopter to leave the branch. We demonstrated that the gripper could effectively support its weight and the weight of the DJI Mavic Mini in the upside-down configuration.

We placed a 250-g weight to determine the duration needed to deplete the 260-mAh battery (movie S5). The gripper consisted of a two-way, normally open solenoid valve (fig. S17). Electrical energy was required to keep the valve closed when perching. Using a digital multimeter, we recorded a reading of 60 mA when the valve was closed. In addition, all pressurized systems lost pressure over time, albeit slowly. Our FiBa modules also lost pressure over time, likely because of the gas permeability through silicone. This pressure loss resulted in the gripper losing its grip. We programmed the micropump to be activated for 2 s after an interval of 5 min to replenish the loss of air pressure. We recorded a current reading of 250 mA when the pump was activated. When a 260-mAh, 3.7-V battery (~9 g) was used, the gripper could hold a weight of 250 g for 3 hours and 14 min before the battery was depleted (movie S5 and fig. S19). In comparison, the DJI Mavic Mini only has a flight time of 30 min (measured while flying at 14 km/hour in windless conditions) when using a 1100-mAh, 7.4-V battery (~100 g). We note that the existing power management design for the gripper is not yet optimized (which is not within the scope of this study). As such, some improvement in grip duration could be anticipated with various modifications. For example, a normally open valve can be replaced with a normally closed valve to further save energy. A closed-loop pressure sensor could also be incorporated to measure the pressure loss within the pneu-nets and only activate the pump when the pressure falls below a threshold value.

To the best of our knowledge, the ability to reduce the weight of an untethered pneu-net soft gripper to a level suitable to be mounted on a small-scale quadcopter has had limited demonstration in literature. This work provides a demonstration of using soft robotic grippers to perch on a branch or pole to save energy, which has immediate potential for practical applications. For example, the soft gripper could be immediately mounted on any existing drones to perch on hard-to-reach places (for example, oil rigs, electric transmission towers, disaster zones) for remote sensing, inspection, and search and rescue operations. Furthermore, the benefit of a soft robotic gripper over conventional rigid joints is its ability to automatically conform itself to objects it is grasping onto. For instance, the gripper could grip branches or bars of various sizes without any preprogramming (fig. S20).

Ladybug-inspired flying robot

In practical applications, it is often necessary for objects to be large and sheetlike at the destination but small and compact during transportation. For example, in the recently launched James Webb Telescope, the sunshield was folded to fit into a rocket for the journey and then deployed once in space (*58*, *59*). Similarly, in nature, we observe examples such as the ladybug, which tucks its wings neatly into a compact form when not in flight (*60*–*62*). When the ladybug intends to fly, it unfolds its wings into a sheetlike structure (Fig. 6A). To provide stiffness and strength to its wings when opened, the cross sections have a characteristic transversal curved shape (*60*). Inspired by nature, we applied similar principles to create an autonomous unfolding wing with the characteristic surface curvature that enhanced the wing stiffness and strength. We used the design principle of structural rigidity by curvature to create sufficient stiffness and strength for flight. By using our FiBa variable stiffness beam modules as the primary structural component of the wing, we made the wing readily collapsible when the embedded balloons were not inflated, allowing rolling and folding. Figure 6B suggests that the wing could be rolled and folded to a compact footprint (length = 140 mm) suitable for transportation when the balloons in the FiBa variable stiffness beam modules were not inflated. When the balloons in the variable stiffness beam were inflated, the wingspan was extended to 375 mm (Fig. 6C). Crucially, we showed that the variable stiffness wing had sufficient stiffness and strength to hold a load (motor and propeller) of 7 g when suspended as a cantilever from one end.

To demonstrate its flight capability, we replaced the wing component of the single actuator monocopter (*63*) with our foldable wing (Fig. 6Di). The foldable wing was fabricated using thin-film polymer sheets [polyethylene terephthalate (PET)] and FiBa variable stiffness beams. The detailed assembly of the robot (fig. S21) and the fluidic connection (fig. S22) are illustrated in the Supplementary Materials. Two FiBa variable stiffness beam modules were included in the wing, highlighted in pink (Fig. 6D). The two FiBa variable stiffness beams provided structural rigidity crucial to flight (Fig. 6Dii). In addition, the FiBa variable stiffness beam functioned as the actuating unit that autonomously unfolded the wing before flight. Next, we included an airfoil segment to the wing as highlighted in turquoise (Fig. 6D). The airfoil segment consisted of a series of tubular balloons coupled together embedded inside the polymer thin film (fig. S21, C to E). The airfoil segment serves two main purposes: It provides a quasi-airfoil profile to enhance lift generation during flight and acts as a structural element to prevent torsional forces. Lastly, a motor with a propeller was attached to the end of the wing (Fig. 6Div).

We demonstrated the ability to unfold the wing autonomously (Fig. 6E, i to v) and immediately transit to flight (Fig. 6Evi and movie S7). The monocopter flies by spinning about its center of gravity, similar to the naturally occurring flight of the maple seed. Its thrust unit (the motor with propeller) provides both thrust to maintain the spin rate and control in five degrees of freedom. The inflated wing provides the necessary aerodynamic forces and torque at an appropriate spin rate to keep the craft aloft and maintain an appropriate pose. To increase altitude, the thrust unit increases thrust, causing the monocopter to spin faster and generate more lift from its wing. To move laterally, the thrust unit is modulated cyclically at every rotation, creating an imbalance in the lift, which tilts the rotation plane of the monocopter and causes it to move in the desired direction.

A monocopter with a semirigid foldable wing was presented in our previous work (*64*). The semirigid foldable wing required human intervention to perform the unfolding process. Because the wing consisted of strips of balsa wood joined together with laminated plastics, it could only be folded in a predetermined configuration. The current wing construction was completely soft, suggesting that it could be folded, rolled, and even crushed when the modular balloons were not inflated. Crucially, the current work allows for autonomous unfolding, unlocking new possibilities such as deploying the folded monocopter mid-air, unfolding itself, and transitioning into flight. In addition, by regulating the structure of tubular sections in the wing section, it is possible to shape them into the desired airfoil type, which can increase the efficiency of the flight.

CONCLUSION

This paper presents a unique approach to fabricating lightweight and untethered soft robots capable of mimicking a range of locomotion found in nature using FiBa modules. The FiBa modules were designed to overcome the weight limitation of conventional silicone-based actuators, enabling untethered operations for soft robots. By combining thin-film polymer sheets with 3D-printed silicone balloons, the FiBa modules substantially reduced the weight of the robots while maintaining their functionality. Four modes of untethered locomotion were demonstrated in this paper: turtle-inspired crawling, inchworm-inspired climbing, bat-inspired perching, and ladybug-inspired flying. The versatility of this approach to constructing soft robots can be instrumental in resource-constrained settings (such as rural areas and space exploration). A wide range of locomotion modes can be replicated by using a core set of commercial electronic components (for example, batteries, valves, pumps, and microcontrollers) and raw structural materials (for example, polymer thin film and modular balloons). There are limited demonstrations of an untethered soft robot light enough to be efficiently coupled to aerial machines. The ability to add perching capabilities to existing quadcopters should find immediate applications in remote sensing, inspection, and search and rescue missions. The autonomous unfolding of a soft wing could open new avenues, such as the deployment of a folded-wing payload from high altitudes and the subsequent autonomous unfolding of its wing to initiate controlled flight and landing.

This study demonstrates a tool for designing and customizing lightweight, untethered soft robots with advanced functionalities. Beyond reducing weight, FiBa modules offer the unique advantages of tuning beam stiffness and enabling shape morphing through unfolding. These capabilities allow for adaptable performance across a wide range of applications. The customizable design and ease of

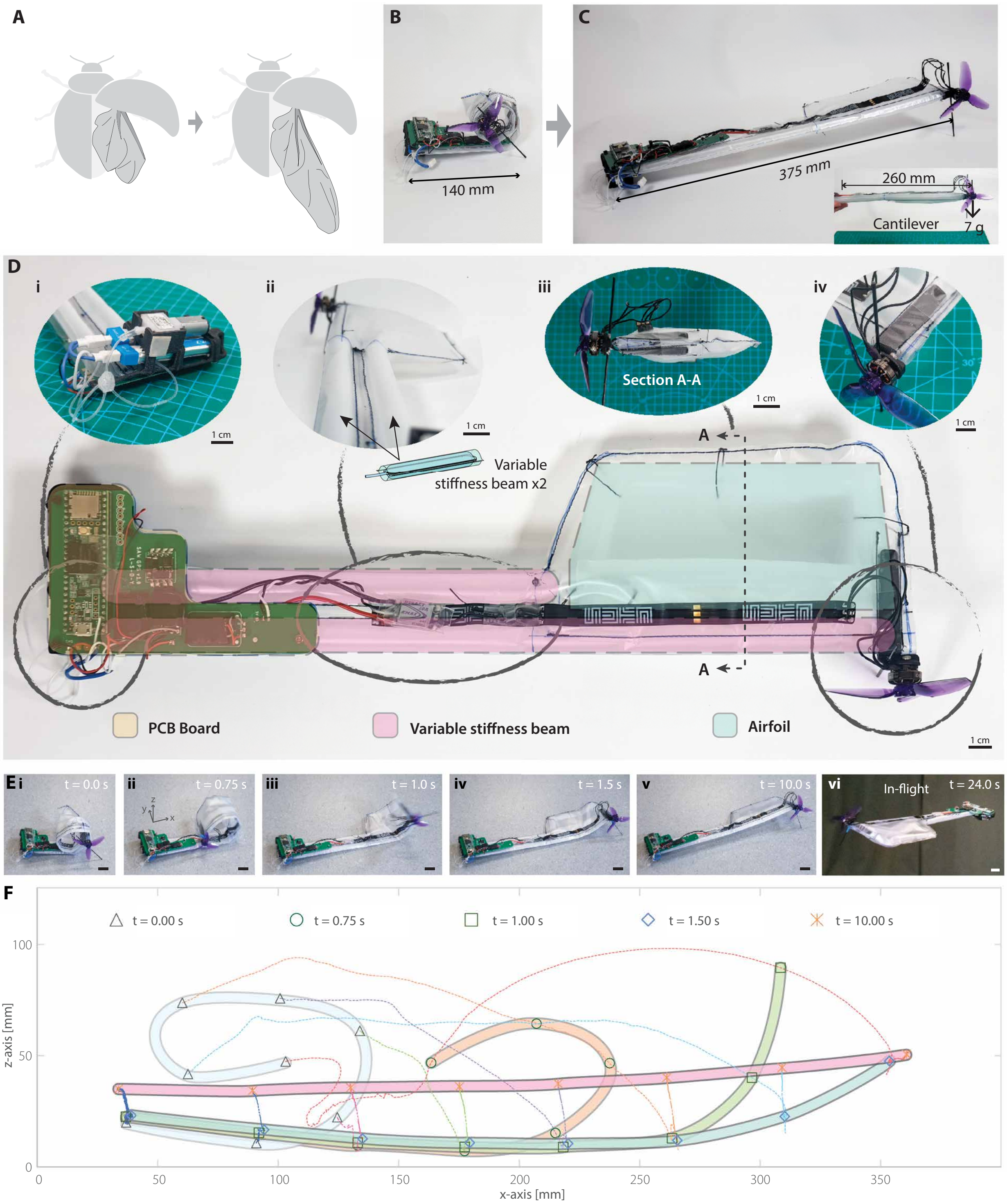

Fig. 6. Ladybug-inspired unfolding wings. (**A**) Illustration of a ladybug unfolding its wings. (**B**) Photograph of the soft-wing monocopter in the folded state. (**C**) Photograph of the soft-wing monocopter in the extended state. (**D**) Top view photograph of the monocopter and the corresponding photographs highlighting the (i) PCB mount, (ii) variable stiffness beams, (iii) airfoil module, and (iv) trust unit. (**E**) Time-lapse image of the monocopter undergoing autonomous unfolding and subsequently transiting into flight. (**F**) *Z-X* coordinates of the optical marker mounted on the wing during autonomous unfolding at selected time points (tracked using the OptiTrack motion capture system). Dotted lines represent the paths taken by each optical marker, and the solid lines illustrate the shape of the wing at each given time point. Scale bar, 1 cm (D); 2 cm (E).

fabrication inherent to the modularity of FiBa units offer roboticists a practical and cost-effective solution. In addition, the energy efficiency of the system due to the reduced weight contributes to prolonged untethered operation, making FiBa modules well suited for applications ranging from disaster relief and space exploration to search and rescue operations. The reduced weight should not only enable seamless integration of additional components but also facilitate the exploration of innovative designs, broadening the spectrum of practical applications in soft robotics.

MATERIALS AND METHODS

Materials

Ecoflex 00-50, Dragon Skin 30, and Sil-Poxy were purchased from Smooth-On (Macungie, PA, USA). Clear PVC binding sheets (A3, thickness = 0.18 mm) were purchased from Art Friend (Singapore, Singapore). PET films (laminating pouch, A3) were purchased from General Binding Corporation (Northbrook, IL, USA). Tapered nozzles were purchased from Aliexpress (Hangzhou, China).

Fabrication of modular balloons

The modular balloons were fabricated using protocols developed in previous works (*65*). Briefly, silicone adhesive was loaded into a pneumatic syringe and mounted on the direct ink writing printer (SHOTmini200SX, Musashi Engineering, Tokyo, Japan). A tapered nozzle of 22G was fitted to the pneumatic syringe. The toolpath was first designed in Rhinoceros (Robert McNeel & Associates, Seattle, WA, USA) and was converted to the MuCAD format (proprietary format for Musashi dispenser analogous to Gcode) using a script written in Grasshopper (Robert McNeel & Associates, Seattle, WA, USA). A silicone sheet was placed on the print bed, and the silicone adhesive was printed on the silicone sheet. Next, silicone tubing was positioned over the printed line. Another layer of silicone sealant was printed over the first to ensure that the adhesive completely covered the silicone tube. Last, a second sheet of silicone was gently placed on the printed pattern and allowed to cure for 24 hours. The silicone sheets for the circular balloons were cast between two glass panels (20 mm by 20 mm). A PVC sheet was placed on the first glass panel to facilitate easy demolding of the silicone sheet. To ensure that the PVC sheet was completely flat against the glass panel (with no trapped pockets of air), we first sprayed a thin coat of water on the glass panel before placing the PVC sheet over it. Trapped air bubbles between the two surfaces were removed by gentle rolling using a roller. Next, uncured Dragon Skin 30 was poured on the panel with the PVC sheet. Then, spacers of 0.77 mm were positioned at all four corners, and the second glass panel was slowly angled over the uncured Dragon Skin 30, ensuring that no air bubbles were trapped in the process. A heavy object was placed over the second glass panel to press out any remaining uncured Dragon Skin 30. The silicone sheets were cast between two A3-sized polymethyl methacrylate sheets for the tubular balloons. Spacers with a thickness of 0.3 mm were used. The spacers were created by layering six layers of Scotch Magic tape (3M, Saint Paul, MN, USA).

Design and fabrication of turtle, inchworm, and perching robot

The robot frames were fabricated using PVC sheets (thickness = 0.18 mm). Cutting files were first designed in Rhinoceros (Robert McNeel & Associates, Seattle, WA, USA) and converted to .dxf format CAD files, as required by the cutting plotter software. The .dxf files were then imported to the cutting plotter software Silhouette Studio (Silhouette America Inc., Lindon, UT, USA). The sheets were cut using the Silhouette Cameo 2 (Silhouette America Inc., Lindon, UT, USA). After cutting, all the parts were snap-fitted together with the self-locking mechanism incorporated in the design of the sheets (fig. S3). The illustrations for assembly and fluidic connection of the robots are summarized [figs. S9 to S11 (turtle), figs. S13 to S15 (inchworm), and figs. S16 and S17 (perching gripper)].

Design and fabrication of the ladybug-inspired wing

The wing was fabricated using PET films (thickness = 0.05 mm). Markings were measured by hand on the PET film to indicate the sewing lines (fig. S21A). First, part no. 1 was sewn onto part no. 2 along the sewing lines, as shown in fig. S21A using a sewing machine (Janome HD5000, Tokyo, Japan). Next, part no. 2 was sewn onto part no. 3. Last, part no. 3 was folded and sewn to create the sleeves for the modular balloons (fig. S21A). To facilitate the insertion of the modular balloon into the sleeves, the balloons were first coated with a thin coating of talcum powder (Johnson & Johnson, New Brunswick, NJ, USA) to minimize the friction between the silicone and the PET sheets. The modular balloons were pneumatically coupled as illustrated (figs. S1 and S22).

The design of the flying craft follows closely the original design and mechanical makeup described in (*63*). A printed circuit board (PCB) mounts and connects the avionics (microcontroller, electronic compass, voltage regulator, radio receiver, and battery) and provides structure to the main body of the craft. Holes were punched in specified locations on the fabricated wing using a 2-mm biopsy punch to allow the PCB to be securely fastened to the wing using mechanical fasteners. The pneumatic pump was mounted underneath the PCB with two key design considerations: meeting the center of gravity requirements for monocopter flight and minimizing interference with the electronic compass.

Statistical analysis

All error bars in this paper were calculated using the SEM for each condition, reflecting the variability of the data. Statistical differences among conditions were assessed using two-sample t tests. Levels of significance are indicated by asterisks: $****P < 0.0001$, $***P < 0.001$, $**P < 0.01$, $*P < 0.05$, and ns, nonsignificant outcomes ($P \geq 0.05$).

Supplementary Materials

The PDF file includes:

Figs. S1 to S24
Table S1
Methods

Other Supplementary Material for this manuscript includes the following:

Movies S1 to S7

REFERENCES AND NOTES

1. F. Iida, C. Laschi, Soft robotics: Challenges and perspectives. *Procedia Comput. Sci.* **7**, 99–102 (2011).
2. F. Chen, M. Y. Wang, Design optimization of soft robots: A review of the state of the art. *IEEE. Robot. Autom. Mag.* **27**, 27–43 (2020).
3. G. Bao, H. Fang, L. Chen, Y. Wan, F. Xu, Q. Yang, L. Zhang, Soft robotics: Academic insights and perspectives through bibliometric analysis. *Soft Robot.* **5**, 229–241 (2018).

4. S. Pfeil, M. Henke, K. Katzer, M. Zimmermann, G. Gerlach, A worm-like biomimetic crawling robot based on cylindrical dielectric elastomer actuators. *Front. Robot. AI* **7**, 9 (2020).
5. R. Xie, M. Su, Y. Zhang, M. Li, H. Zhu, Y. Guan, PISRob: A pneumatic soft robot for locomoting like an inchworm, in *2018 IEEE International Conference on Robotics and Automation (ICRA)* (IEEE, 2018), pp. 3448–3453.
6. M. Wehner, R. L. Truby, D. J. Fitzgerald, B. Mosadegh, G. M. Whitesides, J. A. Lewis, R. J. Wood, An integrated design and fabrication strategy for entirely soft, autonomous robots. *Nature* **536**, 451–455 (2016).
7. C. Laschi, B. Mazzolai, M. Cianchetti, Soft robotics: Technologies and systems pushing the boundaries of robot abilities. *Sci. Robot.* **1**, eaah3690 (2016).
8. C. S. X. Ng, G. Z. Lum, Untethered soft robots for future planetary explorations? *Adv. Intell. Syst.* **5**, 2100106 (2023).
9. N. El-Atab, R. B. Mishra, F. Al-Modaf, L. Joharji, A. A. Alsharif, H. Alamoudi, M. Diaz, N. Qaiser, M. M. Hussain, Soft actuators for soft robotic applications: A review. *Adv. Intell. Syst.* **2**, 2000128 (2020).
10. E. W. Hawkes, C. Majidi, M. T. Tolley, Hard questions for soft robotics. *Sci. Robot.* **6**, eabg6049 (2021).
11. S. I. Rich, R. J. Wood, C. Majidi, Untethered soft robotics. *Nat. Electron.* **1**, 102–112 (2018).
12. G.-Z. Yang, J. Bellingham, P. E. Dupont, P. Fischer, L. Floridi, R. Full, N. Jacobstein, V. Kumar, M. McNutt, R. Merrifield, B. J. Nelson, B. Scassellati, M. Taddeo, R. Taylor, M. Veloso, Z. L. Wang, R. Wood, The grand challenges of *Science Robotics*. *Sci. Robot.* **3**, eaar7650 (2018).
13. X. Huang, K. Kumar, M. K. Jawed, A. M. Nasab, Z. Ye, W. Shan, C. Majidi, Chasing biomimetic locomotion speeds: Creating untethered soft robots with shape memory alloy actuators. *Sci. Robot.* **3**, eaau7557 (2018).
14. M. Malley, M. Rubenstein, R. Nagpal, Flippy: A soft, autonomous climber with simple sensing and control, in *2017 IEEE/RSJ International Conference on Intelligent Robots and Systems (IROS)* (IEEE, 2017), pp. 6533–6540.
15. M. T. Tolley, R. F. Shepherd, B. Mosadegh, K. C. Galloway, M. Wehner, M. Karpelson, R. J. Wood, G. M. Whitesides, A resilient, untethered soft robot. *Soft Robot.* **1**, 213–223 (2014).
16. M. T. Tolley, R. F. Shepherd, M. Karpelson, N. W. Bartlett, K. C. Galloway, M. Wehner, R. Nunes, G. M. Whitesides, R. J. Wood, An untethered jumping robot, in *2014 IEEE/RSJ International Conference on Intelligent Robots and Systems* (IEEE, 2014), pp. 561–566.
17. H.-T. Lin, G. G. Leisk, B. Trimmer, GoQBot: A caterpillar-inspired soft-bodied rolling robot. *Bioinspir. Biomim.* **6**, 026007 (2011).
18. D. Drotman, S. Jadhav, D. Sharp, C. Chan, M. T. Tolley, Electronics-free pneumatic circuits for controlling soft-legged robots. *Sci. Robot.* **6**, eaay2627 (2021).
19. C. A. Aubin, B. Gorissen, E. Milana, P. R. Buskohl, N. Lazarus, G. A. Slipher, C. Keplinger, J. Bongard, F. Iida, J. A. Lewis, R. F. Shepherd, Towards enduring autonomous robots via embodied energy. *Nature* **602**, 393–402 (2022).
20. D. Rus, M. T. Tolley, Design, fabrication and control of soft robots. *Nature* **521**, 467–475 (2015).
21. B. Mosadegh, P. Polygerinos, C. Keplinger, S. Wennstedt, R. F. Shepherd, U. Gupta, J. Shim, K. Bertoldi, C. J. Walsh, G. M. Whitesides, Pneumatic networks for soft robotics that actuate rapidly. *Adv. Funct. Mater.* **24**, 2163–2170 (2014).
22. R. F. Shepherd, F. Ilievski, W. Choi, S. A. Morin, A. A. Stokes, A. D. Mazzeo, X. Chen, M. Wang, G. M. Whitesides, Multigait soft robot. *Proc. Natl. Acad. Sci. U.S.A.* **108**, 20400–20403 (2011).
23. F. Ilievski, A. D. Mazzeo, R. F. Shepherd, X. Chen, G. M. Whitesides, Soft robotics for chemists. *Angew. Chem. Int. Ed. Engl.* **50**, 1890–1895 (2011).
24. R. V. Martinez, J. L. Branch, C. R. Fish, L. Jin, R. F. Shepherd, R. M. D. Nunes, Z. Suo, G. M. Whitesides, Robotic tentacles with three-dimensional mobility based on flexible elastomers. *Adv. Mater.* **25**, 205–212 (2013).
25. S. A. Morin, R. Shepherd, S. W. Kwok, A. A. Stokes, A. Nemiroski, G. M. Whitesides, Camouflage and display for soft machines. *Science* **337**, 828–832 (2012).
26. Z. Wang, P. Polygerinos, J. T. B. Overvelde, K. C. Galloway, K. Bertoldi, C. J. Walsh, Interaction forces of soft fiber reinforced bending actuators. *IEEE ASME Trans. Mechatron.* **22**, 717–727 (2017).
27. K. C. Galloway, P. Polygerinos, C. J. Walsh, R. J. Wood, Mechanically programmable bend radius for fiber-reinforced soft actuators, in *2013 16th International Conference on Advanced Robotics (ICAR)* (IEEE, 2013), pp. 1–6.
28. F. Connolly, C. J. Walsh, K. Bertoldi, Automatic design of fiber-reinforced soft actuators for trajectory matching. *Proc. Natl. Acad. Sci. U.S.A.* **114**, 51–56 (2017).
29. G. Singh, G. Krishnan, Designing fiber-reinforced soft actuators for planar curvilinear shape matching. *Soft Robot.* **7**, 109–121 (2020).
30. Q. Wei, H. Xu, F. Sun, F. Chang, S. Chen, X. Zhang, Biomimetic fiber reinforced dual-mode actuator for soft robots. *Sens. Actuators. A Phys.* **344**, 113761 (2022).
31. P. Polygerinos, Z. Wang, K. C. Galloway, R. J. Wood, C. J. Walsh, Soft robotic glove for combined assistance and at-home rehabilitation. *Rob. Auton. Syst.* **73**, 135–143 (2015).
32. M. Schaffner, J. A. Faber, L. Pianegonda, P. A. Rühs, F. Coulter, A. R. Studart, 3D printing of robotic soft actuators with programmable bioinspired architectures. *Nat. Commun.* **9**, 878 (2018).
33. Z. Wang, B. Zhang, Q. He, H. Chen, J. Wang, Y. Yao, N. Zhou, W. Cui, Multimaterial embedded 3D printing of composite reinforced soft actuators. *Research* **6**, 0122 (2023).
34. J. D. Hubbard, R. Acevedo, K. M. Edwards, A. T. Alsharhan, Z. Wen, J. Landry, K. Wang, S. Schaffer, R. D. Sochol, Fully 3D-printed soft robots with integrated fluidic circuitry. *Sci. Adv.* **7**, eabe5257 (2021).
35. D. Yang, M. S. Verma, J.-H. So, B. Mosadegh, C. Keplinger, B. Lee, F. Khashai, E. Lossner, Z. Suo, G. M. Whitesides, Buckling pneumatic linear actuators inspired by muscle. *Adv. Mater. Technol.* **1**, 1600055 (2016).
36. B. Gorissen, D. Melancon, N. Vasios, M. Torbati, K. Bertoldi, Inflatable soft jumper inspired by shell snapping. *Sci. Robot.* **5**, eabb1967 (2020).
37. R. V. Martinez, C. R. Fish, X. Chen, G. M. Whitesides, Elastomeric origami: Programmable paper-elastomer composites as pneumatic actuators. *Adv. Funct. Mater.* **22**, 1376–1384 (2012).
38. A. Pagano, T. Yan, B. Chien, A. Wissa, S. Tawfick, A crawling robot driven by multi-stable origami. *Smart Mater. Struct.* **26**, 094007 (2017).
39. S. Li, D. M. Vogt, D. Rus, R. J. Wood, Fluid-driven origami-inspired artificial muscles. *Proc. Natl. Acad. Sci. U.S.A.* **114**, 13132–13137 (2017).
40. L. Paez, G. Agarwal, J. Paik, Design and analysis of a soft pneumatic actuator with origami shell reinforcement. *Soft Robot.* **3**, 109–119 (2016).
41. V. Sanchez, K. Mahadevan, G. Ohlson, M. A. Graule, M. C. Yuen, C. B. Teeple, J. C. Weaver, J. McCann, K. Bertoldi, R. J. Wood, 3D knitting for pneumatic soft robotics. *Adv. Funct. Mater.* **33**, 2212541 (2023).
42. Y. Luo, K. Wu, A. Spielberg, M. Foshey, D. Rus, T. Palacios, W. Matusik, Digital fabrication fo pneumatic actuators with integrated sensing by machine knitting, in *Proceedings of the 2022 CHI Conference on Human Factors in Computing Systems* (ACM, 2022), pp. 1–13.
43. L. Cappello, K. C. Galloway, S. Sanan, D. A. Wagner, R. Granberry, S. Engelhardt, F. L. Haufe, J. D. Peisner, C. J. Walsh, Exploiting textile mechanical anisotropy for fabric-based pneumatic actuators. *Soft Robot.* **5**, 662–674 (2018).
44. J. Meng, J. Buzzatto, Y. Liu, M. Liarokapis, On aerial robots with grasping and perching capabilities: A comprehensive review. *Front. Robot. AI* **8**, 739173 (2022).
45. V. Pini, J. J. Ruz, P. M. Kosaka, O. Malvar, M. Calleja, J. Tamayo, How two-dimensional bending can extraordinarily stiffen thin sheets. *Sci. Rep.* **6**, 29627 (2016).
46. G. Knott, A. Viquerat, Curved bistable composite slit tubes with positive Gaussian curvature. *AIAA J.* **56**, 1679–1688 (2018).
47. L. Giomi, L. Mahadevan, Multi-stability of free spontaneously curved anisotropic strips. *Proc. R. Soc. A* **468**, 511–530 (2012).
48. M. Taffetani, F. Box, A. Neveu, D. Vella, Limitations of curvature-induced rigidity: How a curved strip buckles under gravity. *Europhys. Lett.* **127**, 14001 (2019).
49. E. H. Mansfield, Large-deflexion torsion and flexure of initially curved strips. *Proc. R. Soc. Lond. A Math. Phys. Eng. Sci.* **334**, 279–298 (1973).
50. Y. Tang, G. Lin, S. Yang, Y. K. Yi, R. D. Kamien, J. Yin, Programmable kiri-kirigami metamaterials. *Adv. Mater.* **29**, 1604262 (2017).
51. D. R. Merritt, F. Weinhaus, The pressure curve for a rubber balloon. *Am. J. Phys.* **46**, 976–977 (1978).
52. I. Müller, H. Struchtrup, Inflating a rubber balloon. *Math. Mech. Solids* **7**, 569–577 (2002).
53. Z. Ješková, D. Featonby, V. Feková, Balloons revisited. *Phys. Educ.* **47**, 392 (2012).
54. D. P. Holland, E. J. Park, P. Polygerinos, G. J. Bennett, C. J. Walsh, The soft robotics toolkit: Shared resources for research and design. *Soft Robot.* **1**, 224–230 (2014).
55. R. V. Martinez, A. C. Glavan, C. Keplinger, A. I. Oyetibo, G. M. Whitesides, Soft actuators and robots that are resistant to mechanical damage. *Adv. Funct. Mater.* **24**, 3003–3010 (2014).
56. W. R. T. Roderick, M. R. Cutkosky, D. Lentink, Bird-inspired dynamic grasping and perching in arboreal environments. *Sci. Robot.* **6**, eabj7562 (2021).
57. M. A. Graule, P. Chirarattananon, S. B. Fuller, N. T. Jafferis, K. Y. Ma, M. Spenko, R. Kornbluh, R. J. Wood, Perching and takeoff of a robotic insect on overhangs using switchable electrostatic adhesion. *Science* **352**, 978–982 (2016).
58. A. Lo, "Engineering the James Webb Space Telescope" in *Frontiers of Engineering: Reports on Leading-Edge Engineering from the 2015 Symposium* (National Academies Press, 2016), pp. 39–44.
59. P. Badagavi, V. Pai, A. Chinta, Use of origami in space science and various other fields of science, in *2017 2nd IEEE International Conference on Recent Trends in Electronics, Information & Communication Technology (RTEICT)* (IEEE, 2017), pp. 628–632.
60. K. Saito, S. Nomura, S. Yamamoto, R. Niiyama, Y. Okabe, Investigation of hindwing folding in ladybird beetles by artificial elytron transplantation and microcomputed tomography. *Proc. Natl. Acad. Sci. U.S.A.* **114**, 5624–5628 (2017).
61. Z. Song, Y. Yan, J. Tong, J. Sun, Asian ladybird folding and unfolding of hind wing: Biomechanical properties of resilin in affecting the tensile strength of the folding area. *J. Mater. Sci.* **55**, 4524–4537 (2020).
62. R. Ishiguro, T. Kawasetsu, Y. Motoori, J. Paik, K. Hosoda, Earwig-inspired foldable origami wing for micro air vehicle gliding. *Front. Robot. AI* **10**, 1255666 (2023).

63. L. S. T. Win, S. K. H. Win, D. Sufiyan, G. S. Soh, S. Foong, Achieving efficient controlled flight with a single actuator, in *2020 IEEE/ASME International Conference on Advanced Intelligent Mechatronics (AIM)* (IEEE, 2020), pp. 1625–1631.
64. S. K. H. Win, L. S. T. Win, D. Sufiyan, S. Foong, Design and control of the first foldable single-actuator rotary wing micro aerial vehicle. *Bioinspir. Biomim.* **16**, 066019 (2021).
65. T. Ching, Y. Li, R. Karyappa, A. Ohno, Y.-C. Toh, M. Hashimoto, Fabrication of integrated microfluidic devices by direct ink writing (DIW) 3D printing. *Sens. Actuators B Chem.* **297**, 126609 (2019).

Acknowledgments

Funding: T.C. thanks the Ministry of Education (MOE), Singapore, for awarding the President's Graduate Fellowship. M.H. thanks the Agency for Science, Technology and Research (A*STAR) (A1983c0039 and M22K2c0085) and Digital Manufacturing and Design (DManD) Centre at Singapore University of Technology and Design (RGDM1620403) for the project support. **Author contributions:** T.C. conceptualized, designed, and performed all experiments and wrote the paper. J.Z.W.L., S.K.H.W., L.S.T.W., D.S., C.P.X.L., and N.N. contributed to fabrication, experiments, and analysis and collection of data. Y.-C.T. supervised and contributed feedback. S.F. conceptualized, supervised, and provided resources. M.H. conceptualized, supervised, provided funding, resources, and wrote the paper. **Competing interests:** None of the authors has any conflict of interests, financial or otherwise. **Data and materials availability:** All additional data required to evaluate the conclusions of the paper are available within the main text and the Supplementary Materials document and on Zenodo (DOI: 10.5281/zenodo.11514235).

Submitted 23 August 2023
Accepted 20 June 2024
Published 17 July 2024
10.1126/scirobotics.adk4533

Science Robotics

Crawling, climbing, perching, and flying by FiBa soft robots

Terry Ching, Joseph Zhi Wei Lee, Shane Kyi Hla Win, Luke Soe Thura Win, Danial Sufiyan, Charlotte Pei Xuan Lim, Nidhi Nagaraju, Yi-Chin Toh, Shaohui Foong, and Michinao Hashimoto

Sci. Robot. **9** (92), eadk4533. DOI: 10.1126/scirobotics.adk4533

Editor's summary

Many soft robots rely on external electrical or pneumatic power sources accompanied by a physical cumbersome tether limiting the robots' range. To achieve untethered operation, Ching *et al*. combined a three-dimensionally printed pneumatic balloon and a curved polymer film to form a soft actuator termed film-balloon, or FiBa, actuator. These bending actuators are substantially lighter than other pneumatic actuators and can be combined with onboard pneumatic pumps, batteries, and controllers for untethered operation. The versatility of these actuators is demonstrated in various biomimetic robot designs that can crawl, climb, perch, and fly. Untethered robots capable of complex modes of locomotion could prove useful in remote operations such as rescue missions and space exploration.
—Melisa Yashinski

Science Robotics (ISSN 2470-9476) is published by the American Association for the Advancement of Science. 1200 New York Avenue NW, Washington, DC 20005. The title *Science Robotics* is a registered trademark of AAAS.